2018

High-Frequency Thermal-Fluidic Characterization of Dynamic Microchannel Flow Boiling Instabilities: Part 1 - Rapid-Bubble-Growth Instability at the Onset of Boiling

T. A. Kingston

J. A. Weibel
Purdue University, jaweibel@purdue.edu

S V. Garimella
Purdue University, sureshg@purdue.edu

Kingston, T. A.; Weibel, J. A.; and Garimella, S V., "High-Frequency Thermal-Fluidic Characterization of Dynamic Microchannel Flow Boiling Instabilities: Part 1 - Rapid-Bubble-Growth Instability at the Onset of Boiling" (2018). *CTRC Research Publications.* Paper 330.
http://dx.doi.org/https://doi.org/10.1016/j.ijmultiphaseflow.2018.05.007

High-Frequency Thermal-Fluidic Characterization of Dynamic Microchannel Flow Boiling Instabilities: Part 1 - Rapid-Bubble-Growth Instability at the Onset of Boiling[1]

Todd A. Kingston, Justin A. Weibel, and Suresh V. Garimella*
Cooling Technologies Research Center
School of Mechanical Engineering, Purdue University, West Lafayette, Indiana 47907 USA

Abstract

Dynamic flow boiling instabilities are studied experimentally in a single, 500 μm-diameter glass microchannel subjected to a uniform heat flux. Fluid flow is driven through the microchannel in an open-loop test facility by maintaining a constant pressure difference between a pressurized upstream reservoir and a reservoir at the exit that is open to the ambient; the working fluid is HFE-7100. This hydrodynamic boundary condition resembles that of an individual channel in a parallel-channel heat sink where the channel mass flux can vary in time. Simultaneous high-frequency measurement of reservoir, inlet, and outlet pressures, pressure drop, mass flux, inlet and outlet fluid temperatures, and wall temperature is synchronized to high-speed flow visualizations enabling transient characterization of the thermal-fluidic behavior. Part 1 of this study investigates the rapid-bubble-growth instability at the onset of boiling; the effect of flow inertia and inlet liquid subcooling is assessed. The mechanisms underlying the rapid-bubble-growth instability, namely, a large liquid superheat and a large

---

[1] Submitted for review to *International Journal of Multiphase Flow* as Part 1 of two companion papers

* Corresponding author
E-mail addresses: kingston@purdue.edu (T.A. Kingston), jaweibel@purdue.edu (J.A. Weibel), sureshg@purdue.edu (S.V. Garimella)

pressure spike, are quantified; this instability is shown to cause flow reversal and can result in large temperature spikes. Low flow inertia exacerbates the rapid-bubble-growth instability by starving the heated channel of liquid replenishment for longer durations and results in severe temperature increases. In the case of high flow inertia or high inlet liquid subcooling, flow reversal is still observed at the onset of boiling, but results in a minimal wall temperature rise because liquid quickly replenishes the heated channel. A companion paper (Part 2) investigates the effect of flow inertia, inlet liquid subcooling, as well as heat flux on the thermal-fluidic oscillations during time-periodic flow boiling that follows the initial incipience at the onset of boiling considered here.

Graphical Abstract

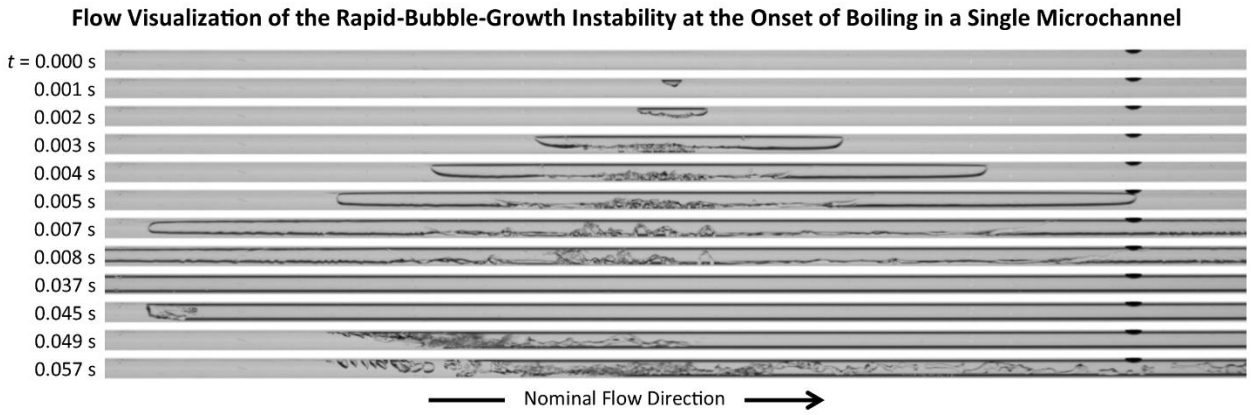

Keywords: dynamic flow boiling instability, microchannel, rapid-bubble-growth instability, two-phase flow

Highlights

- The rapid-bubble-growth instability at the onset of flow boiling is studied.
- The effects of flow inertia and inlet liquid subcooling are investigated.
- Flow visualizations are synchronized to transient thermal-fluidic signatures.

- The rapid-bubble-growth instability at the onset of boiling causes flow reversal.

Nomenclature

c_p	specific heat [J/(kg °C)]
D	microchannel inside diameter [μm]
G	mass flux [kg/m^{2}s]
$G_{1\phi}$	nominal single-phase mass flux [kg/m^{2}s]
h_{fg}	heat of vaporization [J/kg]
k	thermal conductivity [W/(m K)]
Δp	pressure drop across the microchannel [kPa]
p_{in}	inlet pressure [kPa]
p_{out}	outlet pressure [kPa]
P_{in}	power into the microchannel [W]
P_{loss}	power loss to ambient [W]
P_{total}	total power applied [W]
L	microchannel length [m]
L_{heated}	microchannel heated length [m]
t	time [s]
T_{in}	inlet fluid temperature [°C]
T_{out}	outlet fluid temperature [°C]
T_{sat}	fluid saturation temperature [°C]
$T_{sat,out}$	fluid saturation temperature corresponding to outlet pressure [°C]
ΔT_{sub}	inlet liquid subcooling relative to outlet saturation temperature [°C]
T_{wall}	microchannel outside wall temperature [°C]
V	voltage [V]
I	electric current [A]
Q	volumetric flow rate [m^3/s]
$q_{in,avg}$	net heat flux into the microchannel [kW/m^2]

Greek Letters

ρ	density [kg/m^3]

μ dynamic viscosity [kg/(m s)]

σ surface tension [N/m]

1 Introduction

The continued miniaturization of electronic devices will require transformative thermal management strategies that are capable of dissipating high heat fluxes (Agostini *et al.*, 2007; Bar-Cohen *et al.*, 2006; Garimella and Harirchian, 2013; Kandlikar *et al.*, 2013). Tuckerman and Pease (1981) pioneered the use high-aspect-ratio microchannels to dissipate heat fluxes up to 790 W/cm^2 using single-phase water flow. Single-phase flow can be accurately predicted using available modeling tools, making evaluation of heat sink designs straightforward when operated under single-phase flow conditions. The small channel dimensions and high surface area-to-volume ratios found in microchannel heat sinks aid in heat transfer but require a large pumping power to overcome the frictional forces. Flow boiling is an attractive approach for the thermal management of devices generating high heat fluxes because it can be realized at lower pumping power than single-phase flow for a given heat removal rate, due to the utilization of the latent heat of vaporization and high heat transfer coefficients. However, designing heat sinks for two-phase operation and predicting their performance is difficult because of commonly encountered flow boiling instabilities. Flow boiling instabilities can lead to premature critical heat flux relative to the conventional dryout mechanism (Bergles and Kandlikar, 2005). In an effort to better understand these instabilities and their implications, flow boiling instabilities have received significant attention through experimental and theoretical analyses (Kuang *et al.*, 2017; Ruspini *et al.*, 2010; Van Oevelen *et al.*, 2017; Zhang *et al.*, 2009), as well as a number of reviews on the subject (Boure *et al.*, 1973; Kakac and Bon, 2008; Ruspini *et al.*, 2014). A

review of flow boiling instabilities encountered in microchannels, with an emphasis on techniques to mitigate the effects, was recently compiled by Prajapati and Bhandari (2017).

Two classes of flow instabilities have been widely recognized in the literature, static and dynamic. Flow is subjected to a static instability if, when disturbed, its new operating conditions tend asymptotically toward operating conditions that differ from the initial ones (Kakac and Bon, 2008). The threshold of operating conditions at which static instabilities are observed can be predicted using steady-state laws (Akagawa *et al.*, 1971; Boure *et al.*, 1973; Van Oevelen *et al.*, 2017). Flow is subjected to a dynamic instability when there is sufficient interaction between the inertia of the flow and the compressibility of the system, leading to delayed feedback (Kakac and Bon, 2008). Dynamic flow instabilities commonly encountered in microscale applications include the rapid-bubble-growth instability, pressure drop instability (sometimes referred to as the upstream compressible volume instability), and parallel channel instability (Koşar *et al.*, 2006). The rapid-bubble-growth instability at the onset of boiling is investigated in Part 1 of this two-part study.

The one dynamic instability that is unique to microscale flow boiling and not observed in macroscale systems is the rapid-bubble-growth instability (Kuo and Peles, 2008). The small characteristic channel sizes confine vapor bubbles formed during boiling, causing the bubbles to significantly influence the operating characteristics of the system. Barber *et al.* (2011) used *n*-pentane to study bubble growth during microchannel flow boiling and reported that bubble growth can occur in two regimes: (i) free bubble growth, where a spherical bubble grows until it approaches the channel hydraulic diameter, and (ii) confined bubble growth, where the bubble is confined by the channel walls and grows in the axial direction. Barber *et al.* (2011) observed that confined bubble growth led to pressure fluctuations and flow reversal. Two underlying

mechanisms contribute to the rapid-bubble-growth instability, *viz.*, the large liquid superheat needed to induce vapor bubble nucleation and the large pressure spike generated within a microchannel that propagates through the surrounding liquid due to rapid growth of a confined bubble (Kuo and Peles, 2008).

One approach to isolate individual instability types and identify their underlying mechanisms is to investigate a single-channel configuration in which individual mechanisms can be more easily observed. Huh *et al.* (2007) used high-speed imaging to qualitatively observe flow reversal in a single microchannel due to the flow regime transition instability which resulted in the growth of elongated bubbles. This instability was quantified using a relatively low-frequency sensor, and high-frequency flow oscillations associated with individual bubble growth events could not be quantitatively resolved. Wang and Cheng (2008) used a single microchannel with 15 heaters and resistance temperature detectors positioned along its axial length to measure the time-resolved wall temperature and pressure drop during flow boiling with deionized water. They demonstrated that a critical exit vapor quality cutoff separated stable and unstable flow boiling, wherein the stability was judged based on the absence or presence of pressure and temperature fluctuations. Barber *et al.* (2011) used pressure and temperature measurements, synchronized with high-speed flow visualization, to observe the rapid-bubble-growth instability during microchannel flow boiling. A syringe pump was used to deliver a constant mass flux in the experiments.

However, extrapolating the results of single-channel flow instability studies to behavior in parallel microchannel heat sinks is difficult because of potential differences in the hydrodynamic boundary conditions. The constant mass flux used in many single-channel studies (Barber *et al.*, 2011; Barber *et al.*, 2009; Wang and Cheng, 2008) is different from conditions in

an individual channel that is part of a parallel-channel system. The behavior of a single channel in a parallel-channel system does not significantly influence the full set of channels thus resulting in a hydrodynamic boundary condition similar to that of a constant pressure drop. In this parallel-channel configuration, the flow rate through an individual channel can fluctuate significantly, resulting in severe thermal oscillations. In the present study, a constant pressure difference between a pressurized reservoir and the ambient is used to induce fluid flow through a single heated microchannel, which resembles the hydrodynamic boundary conditions of an individual channel in a parallel-channel system. This deliberate choice of boundary conditions in the present study enables the rapid-bubble-growth instability and the pressure drop instability to be studied in the absence of the confounding influence of the parallel channel instability. Part 1 of this two-part study focuses on the rapid-bubble-growth instability at the onset of boiling while Part 2 (Kingston *et al.*, 2017) investigates the instabilities that occur during time-periodic boiling, after the effects of the initial onset have diminished.

High-frequency thermal-fluidic characterization techniques (*e.g.*, measurement of pressure, mass flux, and temperature) are needed to resolve the transient features associated with dynamic flow boiling instabilities. These techniques have been successfully used to quantify the transient heat transfer mechanisms that occur during flow boiling processes. Rao *et al.* (2014) embedded thin-film titanium heaters and thermistors beneath a single microchannel to allow heating and measurement of surface temperatures with high spatial and temporal resolution during flow boiling. Local surface temperatures were significantly influenced by bubble nucleation, thin-film evaporation, and dryout. Bigham and Moghaddam (2015) custom-fabricated a test section that could make temperature measurements at 20,000 Hz using a series of 50 μm-wide resistance temperature detectors, enabling local heat flux measurements with

spatial and temporal resolutions of 40-65 μm and 50 μs, respectively. Local vapor bubble dynamics were shown to influence the instantaneous heat transfer rates and mechanisms.

In Part 1 of this two-part study, high-speed flow visualizations are synchronized to high-frequency pressure, mass flux, and temperature measurements and are used to quantify the underlying mechanisms of the rapid-bubble-growth instability at the onset of flow boiling in a single heated microchannel with hydrodynamic boundary conditions that resemble an individual channel in a parallel-channel system. The transient thermal-fluidic signatures are analyzed to understand the effect of flow inertia and inlet liquid subcooling. In Part 2 (Kingston *et al.*, 2017), the effect of flow inertia, inlet liquid subcooling, and heat flux on the magnitude and frequency of the thermal-fluidic oscillations are quantified during time-periodic flow boiling.

2 Experimental Methods

2.1 Test Facility

The custom-built experimental facility, schematically illustrated in Figure 1, uses a pressurized reservoir to deliver degassed, dielectric HFE-7100 liquid (Novec Engineered Fluid, 3M; fluid properties listed in Table 1) to the test section. The pressure difference between this reservoir and the ambient is used to generate an open-loop flow. The rigid stainless steel reservoir is pressurized by boiling fluid using a submerged cartridge heater (G6A-15568, Watlow). Electrical power is supplied to the cartridge heater using an adjustable direct current (DC) power supply (XG 850W 150-5.6, Sorensen). A constant reservoir pressure is set and maintained by adjusting the amount of power delivered to the cartridge heater.

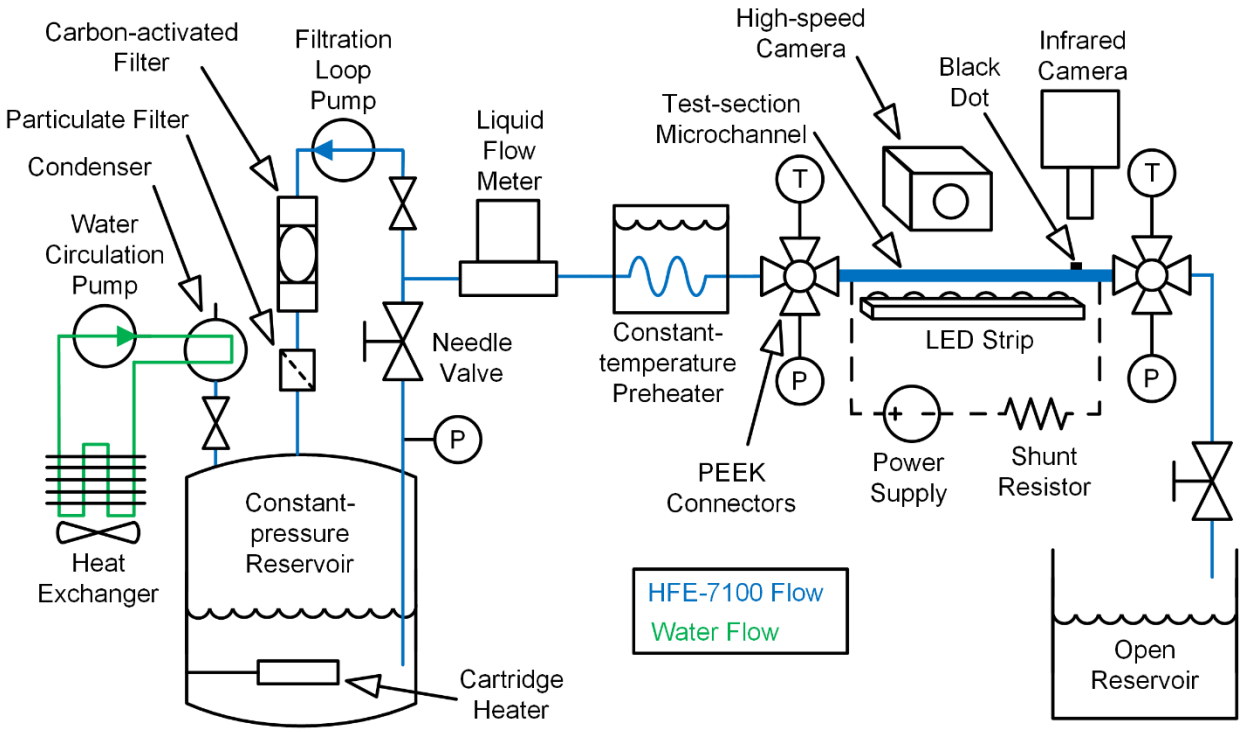

Figure 1. Schematic diagram of the experimental facility featuring a constant pressure reservoir used to deliver fluid flow through the heated test section microchannel.

Table 1. Fluid properties of saturated HFE-7100 at atmospheric pressure (3M, 2002).

	Liquid	Vapor
Density, ρ [kg/m^3]	1399	9.87
Specific heat, c_p [J/(kg °C)]	1255	929
Thermal conductivity, k [W/(m K)]	0.0618	0.0156
Dynamic viscosity, μ [kg/(m s)]	3.61×10^{-4}	1.12×10^{-5}
Heat of vaporization, h_{fg} [J/kg]	— 111600 —	
Saturation temperature, T_{sat} [°C]	—— 61 ——	
Surface tension, σ [N/m]	— 0.0103 —	

Liquid is extracted from the reservoir through an internal dip tube. The liquid flow rate and the test section outlet saturation pressure are adjusted using a pair of needle valves (FVL-404-SS and FVL-405-SS, Omega Engineering), one upstream and one downstream of the test

section, respectively. The liquid volumetric flow rate and temperature are measured using a liquid flow meter (LC-10CCM-D-EPDM, Alicat; accuracy of ±1% full scale). The liquid mass flux is determined using the measured volumetric flow rate and the density corresponding to the measured liquid temperature at that location. The fluid is preheated to the desired inlet temperature immediately upstream of the test section, using a constant-temperature circulating bath (NESLAB EX 17, Thermo Electron Corp.). The inlet and outlet fluid temperatures are measured immediately upstream and downstream of the test section, respectively, using small exposed-tip thermocouples (TMTSS-020E-6, Omega Engineering; accuracy of ±0.5 °C) featuring a bead diameter of ~250 μm, which enables dynamic changes in fluid temperatures to be measured. The pressures at the inlet and outlet of the microchannel are measured using separate pressure transducers (PX309-030G5V and PX309-015G5V, respectively, Omega Engineering; accuracy of ±1%). Short, rigid stainless steel tubes were used to connect the pressure transducers to the polyetheretherketone (PEEK) connectors (ZX2LPK, Valco Instruments) to minimize damping and enable dynamic pressure fluctuations to be accurately measured. Two individual pressure transducers were used instead of a differential pressure transducer to minimize the volume of fluid that would effectively be in parallel with the test section; the pressure measurements were observed to be damped when the use of a differential transducer was explored. The pressure drop across the test section is taken as the difference between the inlet and outlet pressure measurements. The thermocouples and pressure transducers, in addition to the fluid inlet and outlet connections, are mounted to the PEEK connectors, as shown in Figure 1; the test-section microchannel is mounted horizontally between these connectors.

The circular cross-section microchannel is made of borosilicate glass (CV5070, VitroCom) with an inside diameter of D = 500 μm and a wall thickness of 100 μm. The outside surface of the microchannel is custom-coated with an approximately 100 nm-thick layer of indium tin oxide (ITO) using atomic layer deposition (Veeco - CNT). The ITO layer is optically transparent and electrically conductive, enabling visualization of the two-phase flow while subjected to uniform Joule heating. Power is supplied to the ITO coating using an adjustable DC power supply (XG 850W 300V-2.8A, Sorensen). The ITO layer is electrically isolated from the flow loop using non-conductive polytetrafluoroethylene (PTFE) ferrules and PEEK nuts for attachment of the microchannel to the PEEK connectors. Any vapor leaving the test section condenses before discharging as liquid to an open reservoir at ambient pressure.

Pressure, mass flux, and fluid temperature measurements are obtained at 2500 Hz using a high-frequency data acquisition (DAQ) unit (USB-6259, National Instruments). The power to the test section is measured at 0.4 Hz using a separate, high-voltage DAQ (34970A, Agilent). The total heating power (which includes power loss to the ambient) applied to the test section is quantified by measuring the voltage drop across and current through the ITO microchannel coating; the current is obtained from a shunt resistor (6142-1-1000, Empro Shunts). The entire experimental facility is mounted on a damped optical table (VIS3672-PG2-325A, Newport Corp.) to ensure that external vibrations are not transmitted to the components.

The microchannel outside wall temperature is measured at a single fixed location using an infrared (IR) camera (SC7000, FLIR) pointed vertically downward at the microchannel. The IR objective lens (ASIO 4×, Janos Technology, Inc.) is focused on a single black dot painted on the outside surface of the microchannel. This IR imaging configuration enables nonintrusive measurement of the wall temperature without obscuring the flow visualization. Infrared images

were acquired at 500 frames per second (fps) using an image resolution of 80 × 64 pixels. An IR camera integration (*i.e.*, exposure) time of 90 μs was used, which enabled wall temperatures up to approximately 200 °C to be measured before saturating the IR camera sensor.

The flow is visualized from the side of the microchannel using a high-speed camera (VEO710L, Phantom) coupled to a macro lens (AF Micro-Nikkor, Nikon). The opposite side of the microchannel is uniformly backlit using a high-intensity light-emitting diode (LED) strip with an integrated light diffuser (BL168, Advanced Illumination). High-speed optical and IR images were synchronized to pressure, mass flux, and temperature measurements using a pulse generator (565, Berkeley Nucleonics Corp.) to simultaneously trigger both cameras and the high-frequency DAQ unit.

2.2 Test Procedure

Immediately prior to testing, the HFE-7100 fluid was degassed by vigorously boiling the liquid in the reservoir using the submerged cartridge heater. An auxiliary pumped loop circulates water through a condenser (Figure 1) to condense the vapor, which falls back into the reservoir, while non-condensable gases are expelled from the system. While degassing, the HFE-7100 was also circulated through an auxiliary pumped loop containing a 2 μm particulate filter (SS-4TF-2, Swagelok) and an activated-carbon filter (12011 Pall Corporation) to remove any contaminants. After degassing and filtering, the pumps in these auxiliary loops were turned off.

Experiments were initiated by boiling the liquid in the reservoir until it reached a constant reservoir pressure of 190 kPa. Liquid flow was then initiated through the test section at the desired nominal single-phase mass flux while maintaining an average test section outlet saturation pressure of 114 kPa, which corresponds to an outlet saturation temperature of 65 °C,

by adjusting the needle valves. The test facility features a constant pressure drop across the system, not a constant mass flux, and thus a nominal single-phase mass flux is defined based on the value measured prior to the onset of boiling. The constant-temperature bath setpoint was then adjusted to heat the liquid to the desired inlet temperature.

After establishing the desired flow conditions, power was applied to the ITO-coating on the microchannel in increments, allowing for steady-state conditions to be achieved between each set point. At low power conditions, the flow remained in a single phase. At a power level large enough to cause the onset of boiling, all sensor and imaging (IR and optical) data were recorded synchronously immediately before and after incipience, thus capturing this transient event. During this onset of boiling, optical images were acquired at 50,000 fps for a duration of 7.85 s, extending approximately 6 s after boiling was initiated.

2.3 Data Reduction

The wall temperature of the microchannel is determined from measurement of the IR image intensity in a 30 × 24-pixel region in the middle of the black dot painted on the outer wall of the microchannel. This intensity is converted to a temperature using a calibration of the IR camera that was performed after testing was complete. For the calibration, the IR camera is focused on a target surface featuring the same black paint used on the microchannel and was varied from 20 °C to 200 °C in approximately 10 °C increments while recording the image intensity. A unique fourth-order polynomial fit of this temperature versus intensity data for each pixel in the imaging region is used to convert the intensity measured during testing to a microchannel wall temperature. The average wall temperature for each image is then calculated by computing the spatial average from the 30 × 24-pixel region.

A portion of the total power supplied to the ITO coating on the microchannel is lost to the ambient (*i.e.*, not transferred to the fluid through the microchannel wall). This power loss is a function of the channel wall temperature and was calibrated after testing. First, the HFE-7100 was drained from the test-section microchannel and the channel was open to the ambient. Next, electric power levels ranging from 0 - 1.5 W (in approximately 0.1 W increments) were applied to the microchannel. In this configuration, all of the supplied power is lost to the ambient. The wall temperature is measured using the IR camera at each power level and a linear fit is applied: $P_{loss} = 0.0086\ T_{wall} - 0.2188$. This temperature-dependent power loss equation had a coefficient of determination of $R^2 = 0.98$. A time-averaged wall temperature (over each data acquisition time) is used to quantify the power loss that occurs during testing, resulting in different power losses for each operating condition. The power into the microchannel is calculated by subtracting the power loss from the total electric power supplied using $P_{in} = P_{total} - P_{loss}$; power is calculated using $P_{total} = VI$ where V is the voltage applied to the test section and I is the current through the test section. The time-averaged heat flux into the test section is calculated using $q_{in,avg} = P_{in} / (\pi\ D\ L_{heated})$.

The instantaneous mass flux through the test section is calculated using $G = Q\rho / (\pi D^2/4)$ where Q is the measured volumetric flow rate and ρ is the calculated liquid density corresponding to the measured liquid temperature at the flow meter. The inlet liquid subcooling is determined using $\Delta T_{sub} = T_{sat,out,avg} - T_{in}$ where $T_{sat,out,avg}$ is the time-averaged fluid saturation temperature corresponding to the measured pressure at the outlet of the test section and T_{in} is the inlet fluid temperature. The pressure drop across the test section is calculated as the difference between the test section inlet and outlet pressures, $\Delta p = p_{in} - p_{out}$.

2.4 Design of Experiments

Five different combinations of nominal single-phase mass flux and inlet liquid subcooling were investigated in this study, as shown in Table 2. The test procedure described in Section 2.2 was adopted for each combination. In this study, the nominal single-phase mass flux is varied, enabling the effect of flow inertia to be studied, while holding the inlet liquid subcooling constant at ΔT_{sub} = 5 °C. Similarly, the inlet liquid subcooling is varied while holding the nominal single-phase mass flux constant at $G_{1\phi}$ = 400 kg/m^{2}s.

Table 2. Operating conditions used in this study to investigate the rapid-bubble-growth instability.

Nominal Single-Phase Mass Flux, $G_{1\phi}$ [kg/m^{2}s]	Inlet Liquid Subcooling, ΔT_{sub} [°C]
200	5
400	5
400	15
400	35
800	5

3 Results and Discussion

When the flow transitions from single-phase to two-phase, the rapid-bubble-growth instability is observed at the onset of boiling, and is captured in the flow visualizations and transient sensor measurements. Figure 2a shows a series of selected images at the onset of flow boiling obtained by the high-speed camera for a nominal single-phase mass flux of 400 kg/m^{2}s and an inlet liquid subcooling of 5 °C. The nominal flow direction (positive mass flux) is from left to right. The entire heated length of the microchannel (L_{heated} / D = 84) is shown in the

frame; the electrical connections to the ITO coating are just outside the viewing region. Figure 2a (t = 0.024 s) shows the single-phase liquid flow immediately prior to nucleation. The small black dot visible in each image, on the top portion of the channel near the outlet, is the location of the IR wall temperature measurement. The entire microchannel cross-section is shown in each image (A-L) and appears uniformly gray; the wall thickness is virtually unidentifiable in the images at the magnification shown. The reservoir, inlet, and outlet pressures, pressure drop across the channel, mass flux, inlet and outlet fluid temperatures, and wall temperature data recorded immediately before and after the onset of boiling (0 s < t < 0.1 s) are shown in Figure 2b. A longer-timescale plot (0 s < t < 1.0 s) is shown in Figure 2c to illustrate the transition from the onset of boiling to time-periodic boiling. The gray shaded box and dashed vertical lines in Figure 2b correspond to the time instances in Figure 2a when the flow visualizations were captured (images A-L).

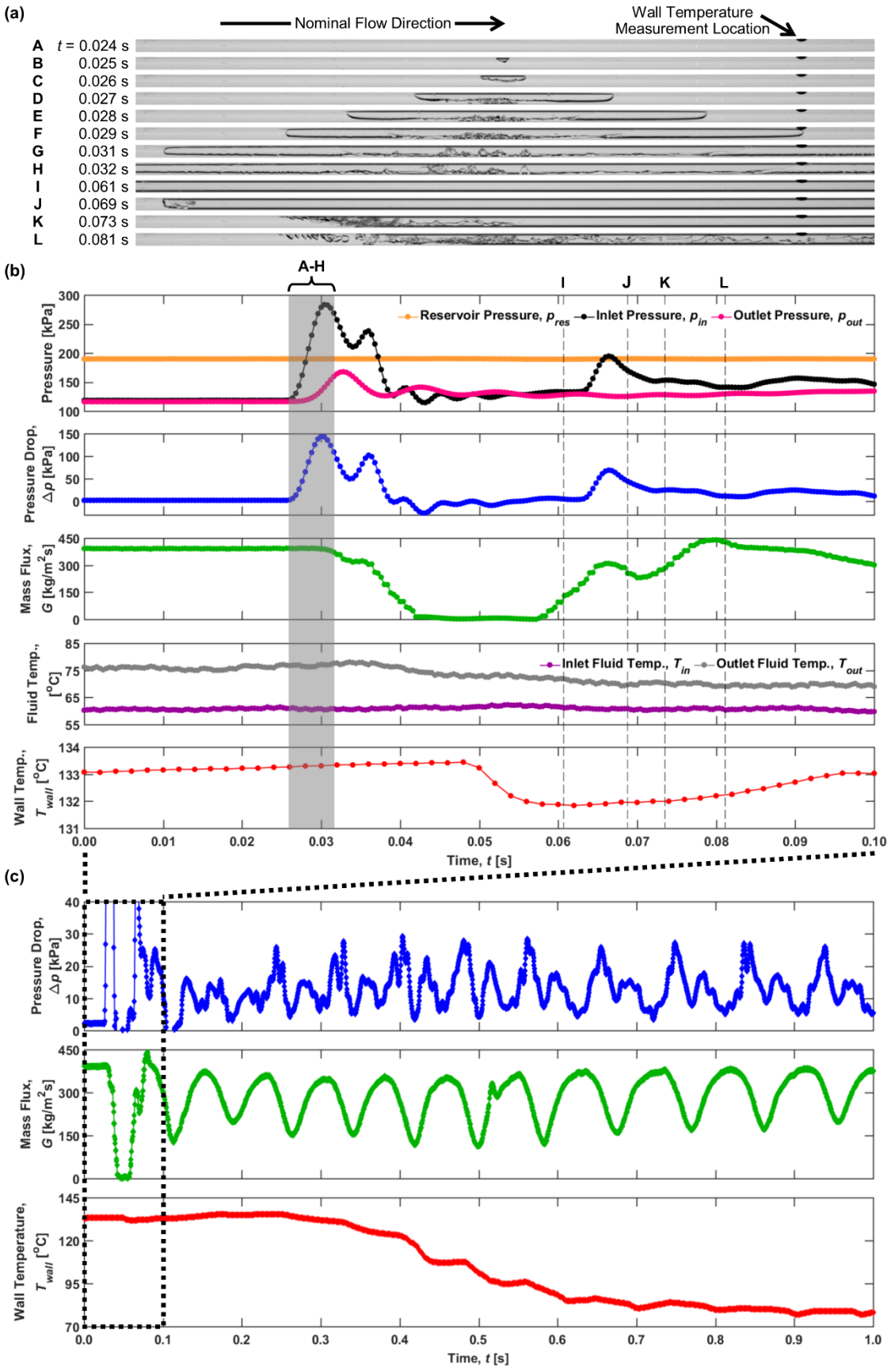
(a)
Nominal Flow Direction
Wall Temperature Measurement Location
A t = 0.024 s
B 0.025 s
C 0.026 s
D 0.027 s
E 0.028 s
F 0.029 s
G 0.031 s
H 0.032 s
I 0.061 s
J 0.069 s
K 0.073 s
L 0.081 s
(b)
A-H
I
J
K
L
Reservoir Pressure, p_{res}
Inlet Pressure, p_{in}
Outlet Pressure, p_{out}
Pressure [kPa]
Pressure Drop, Δp [kPa]
Mass Flux, G [kg/m^{2}s]
Inlet Fluid Temp., T_{in}
Outlet Fluid Temp., T_{out}
Fluid Temp., [^{o}C]
Wall Temp., T_{wall} [^{o}C]
Time, t [s]
(c)
Pressure Drop, Δp [kPa]
Mass Flux, G [kg/m^{2}s]
Wall Temperature, T_{wall} [^{o}C]
Time, t [s]

Figure 2. (a) Selected images of the two-phase morphology during the rapid-bubble-growth instability at the onset of boiling for $G_{1\phi}$ = 400 kg/m^{2}s and ΔT_{sub} = 5 °C, and (b) synchronized measurements of pressure, pressure drop, mass flux, inlet and outlet fluid temperatures, and wall temperature. Images A-L in (a) correspond to the time instances indicated by the gray box (A-H) and dashed vertical lines (I-L) in (b). The nominal flow direction in (a) is from left to right. A corresponding video of the synchronized flow visualizations and thermal-fluidic signatures during the onset of boiling (*i.e.*, Figure 2a and 2b) is available online in the Supplementary Materials (Video S1). (c) The pressure drop, mass flux, and wall temperature measurements are also plotted over a longer timescale showing the transition from the onset of boiling to time-periodic flow boiling.

Prior to nucleation (*i.e.*, during single-phase flow when $q_{in,avg} \leq 33.7$ kW/m^2), all the sensor measurements remain constant in time, as shown in Figure 2b from 0 s < t < 0.024 s. Immediately prior to nucleation, the outlet fluid temperature is 78.0 °C, corresponding to a large liquid superheat of 12.4 °C relative to the outlet saturation temperature of the fluid (65.6 °C). The glass microchannel used in this study has a smooth inside wall and HFE-7100 is a highly wetting liquid; these characteristics impose a large energy barrier for nucleation that typically suppresses vapor bubble formation during boiling until a large liquid superheat is attained, for example, as shown by Kuo and Peles (2008) for the walls of smooth silicon microchannels. At t = 0.025 s, a single vapor bubble nucleates from the top portion of the inside wall of the microchannel near the middle of the heated region (Figure 2a). Nucleation at the onset of boiling preferentially occurred at this location, likely because of a small imperfection on the inside surface. Once formed, the small vapor bubble grows very rapidly both upstream and downstream from the nucleation site. This explosive growth is attributed to the vapor bubble

being surrounded by superheated liquid, which drives rapid liquid-to-vapor phase change and volumetric expansion of the bubble due to the density difference between vapor and liquid. As the vapor bubble becomes circumferentially confined by the microchannel wall, growth predominantly occurs in the axial direction. The furthest upstream and downstream portions of the vapor bubble feature a bullet-like shape, due to the high-velocity (3.5 m/s) propagation of the vapor-liquid interface. Rapid growth of the vapor bubble generates a large pressure spike within the microchannel that also propagates upstream and downstream through the liquid. As shown in Figure 2b, the inlet pressure begins to abruptly increase at t = 0.026 s until it reaches a maximum pressure of 283 kPa at t = 0.030 s. The pressure spike is so large that the inlet pressure exceeds that of the reservoir pressure (190 kPa). Similarly, the outlet pressure begins increasing at t = 0.027 s until it reaches a maximum pressure of 168 kPa at t = 0.033 s. The local spike in pressure promotes flow reversal upstream of the nucleation site. This local pressure spike, combined with the large liquid superheat that drives evaporation and expansion of the bubble, are the underlying mechanisms responsible for the rapid-bubble-growth instability. The faster response and increased pressure magnitude of the inlet pressure, relative to the outlet pressure, is attributed to the inability of the system to relieve the increasing pressure upstream of the rapidly growing vapor bubble. Instead, it begins to pressurize any compressible volume upstream of the test section.

Eventually, the entire heated length of the microchannel is occupied by a long continuous vapor bubble with only a thin layer of liquid separating it from the heated wall (Figure 2a; t = 0.032 s). This time instant approximately corresponds to maxima being observed in the inlet pressure and pressure drop, as shown in Figure 2b. A flow reversal is detected by the upstream flow meter, which measures a change in mass flux from the nominal single-phase flow condition

of 400 kg/m^{2}s to virtually zero at t = 0.042 s and extends until t = 0.057 s (duration of 0.015 s); the flow meter is unable to measure negative flow rates, and shows a zero reading instead.

As the vapor-liquid interface moves downstream, and past the location of the wall temperature measurement (Figure 2a; t = 0.029 s), the liquid begins to cool as the excess sensible heat stored in the superheated liquid is converted to latent heat via evaporation. The outlet fluid temperature eventually decreases to the saturation temperature of the fluid. This process initially begins to cool the microchannel wall, as shown in Figure 2b at t = 0.048 s. There is a 0.019 s delay between the vapor bubble passing the location of the temperature measurement and the wall temperature beginning to decrease, due to the thermal lag in conduction through the channel wall. At later times, the liquid film appears to thin and becomes more spatially uniform (*i.e.*, interfacial waves are eliminated) and the channel is filled with mostly vapor (Figure 2a; t = 0.061 s). Due to starvation of incoming liquid, the wall temperature then begins to increase at t = 0.062 s.

As the pressure wave that was generated at the onset of boiling travels upstream and downstream through the liquid, its magnitude decays and results in a reduction in the inlet and outlet pressures and eventually initiates a measurable mass flux at t = 0.058 s. The pressure build-up in the compressible volume upstream of the test section is relieved, causing the mass flux to increase to a maximum of 440 kg/m^{2}s at t = 0.080 s, exceeding the nominal single-phase mass flux for a brief time. The increased mass flux causes the vapor located upstream of the image frame to be forced back downstream and the furthest upstream portion of the vapor-liquid interface to become visible again within the viewing window (Figure 2b; t = 0.069 s). Small vapor bubbles begin to successively nucleate and depart from the microchannel wall at a fixed axial location (Figure 2b; t = 0.073 s). As these bubbles move downstream and grow, they

coalesce and form larger, confined vapor bubbles resembling a slug flow regime before transitioning to churn and annular flow. After t = 0.081 s, the two-phase morphology begins exhibiting time-periodic fluctuations and the effects of the rapid-bubble-growth instability completely attenuate.

Figure 2c shows the pressure drop, mass flux, and wall temperature data for a longer duration ($0 < t < 1$ s) to illustrate the transition from the onset of boiling to time-periodic boiling; time-periodic oscillations in the pressure drop and mass flux are observed for $t > 0.081$ s (Figure 2c). The thermal response is much slower than the hydrodynamic response due to the thermal capacitance of the microchannel wall, and the wall temperature takes longer to achieve time-periodic behavior (Figure 2c). The wall temperature first increases 2 °C due to the rapid-bubble-growth instability, from 133.4 °C during single-phase flow to a maximum wall temperature of 135.4 °C at t = 0.244 s. It then reduces due to the change in the two-phase morphology and exhibits time-period fluctuations around a mean of 82 °C beginning at approximately t = 0.900 s.

3.1 Effect of Flow Inertia

While the rapid-bubble-growth instability at the onset of boiling for $G_{1\phi}$ = 400 kg/m^{2}s and ΔT_{sub} = 5 °C only resulted in a 2 °C transient increase in the wall temperature relative to single-phase flow that then decayed (Figure 2), this was not always the case. In particular, when the flow inertia was reduced, a larger and longer transient temperature excursion was observed. Figure 3 shows a series of selected images at the onset of flow boiling for a nominal single-phase mass flux of 200 kg/m^{2}s and an inlet liquid subcooling of 5 °C, as well as the synchronized pressure drop, mass flux, and wall temperature measurements before, during, and after the onset of boiling on a longer timescale (0 s < t < 4.5 s). Prior to nucleation, the wall temperature is 119 °C. Once a vapor bubble nucleated from the channel surface (Figure 3; t = 0.299 s), it exhibits

explosive growth both upstream and downstream, as in the discussion above. Similarly, it is accompanied by a large pressure spike and a reduction in the mass flux (Figure 3b) to a value of zero. A mass flux value of zero (indicating flow reversal) is detected for a duration of 0.066 s, a fourfold increase relative to the case with $G_{1\phi}$ = 400 kg/m^{2}s. The wall temperature then begins to increase significantly and reaches a maximum temperature of 163 °C at t = 1.968 s. This larger increase in wall temperature is attributed to the lower flow inertia in this case, which causes flow reversal (as detected by the flow meter) and the initial vapor bubble that fills the channel (Figure 3a) to remain in place for a longer period of time for $G_{1\phi}$ = 200 kg/m^{2}s compared to $G_{1\phi}$ = 400 kg/m^{2}s, starving the heated wall of adequate liquid replenishment. Such significant increases in the wall temperature caused by the rapid-bubble-growth instability could be catastrophic to temperature-sensitive devices. Shortly after the wall reaches its maximum temperature, the flow begins to enter a time-periodic flow boiling condition where oscillations in pressure drop and mass flux are observed (t > ~2.25 s). This cools the microchannel wall and time-periodic wall temperature oscillations centered at ~75 °C begin at approximately t = 4.0 s.

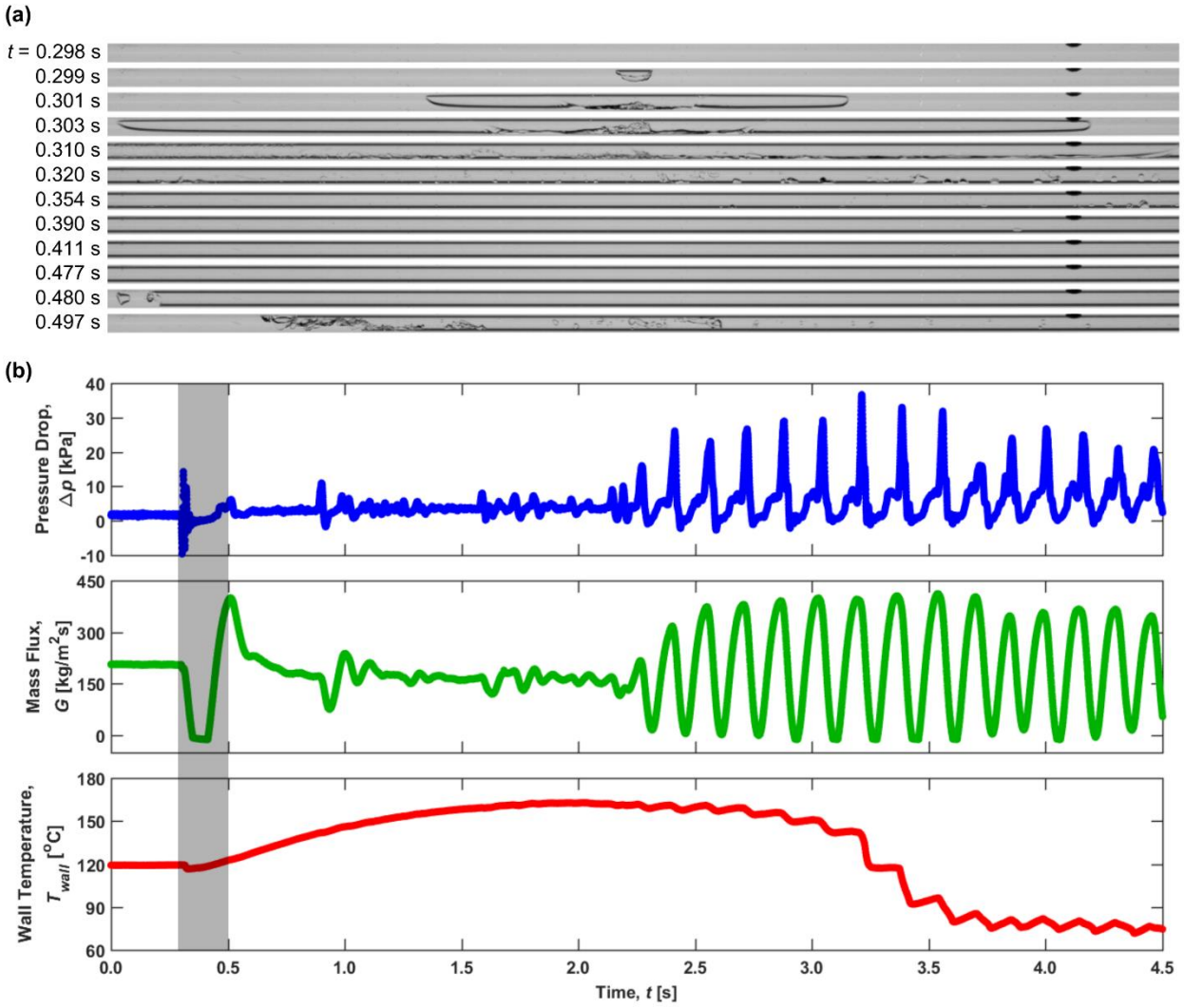

Figure 3. (a) Selected images of the two-phase morphology during the rapid-bubble-growth instability at the onset of boiling for $G_{1\phi}$ = 200 kg/m^{2}s and ΔT_{sub} = 5 °C, and (b) synchronized measurements of pressure drop, mass flux, and wall temperature. Images in (a) correspond to the time instances in the gray box in (b). A corresponding video of the synchronized flow visualizations and thermal-fluidic signatures during the onset of boiling is available online in the Supplementary Materials (Video S2).

For a larger nominal single-phase mass flux of $G_{1\phi}$ = 800 kg/m^{2}s, the effect on the rapid-bubble-growth instability is minimal because the flow inertia is sufficient to mitigate the effects

of flow reversal (as was observed at $G_{1\phi}$ = 400 kg/m^{2}s). The flow meter measured a value of zero (indicating flow reversal) for a duration of 0.015 s when $G_{1\phi}$ = 800 kg/m^{2}s, identical to the case when $G_{1\phi}$ = 400 kg/m^{2}s. At the onset of boiling for $G_{1\phi}$ = 800 kg/m^{2}s, the wall temperature reduced to a much lower value; there was never an increase from its initial temperature during single-phase flow (unlike the brief increase at the onset observed for $G_{1\phi}$ = 400 kg/m^{2}s). A video showing the two-phase morphology synchronized to pressure drop, mass flux, and wall temperature measurements at the onset of boiling for a nominal single-phase mass flux of 800 kg/m^{2}s and ΔT_{sub} = 5 °C is provided online in the Supplementary Materials (Video S3).

3.2 Effect of Inlet Liquid Subcooling

The effect of the inlet liquid subcooling on the rapid-bubble-growth instability was studied by changing the subcooling to ΔT_{sub} = 15 °C and 35 °C while holding the nominal-single phase mass flux constant ($G_{1\phi}$ = 400 kg/m^{2}s). Figure 4 shows a series of selected images at the onset of flow boiling for a nominal single-phase mass flux of 400 kg/m^{2}s and an inlet liquid subcooling of 15 °C, as well as the synchronized pressure drop, mass flux, and wall temperature measurements before, during, and after the onset of boiling on a longer timescale (0 s < t < 2.0 s).

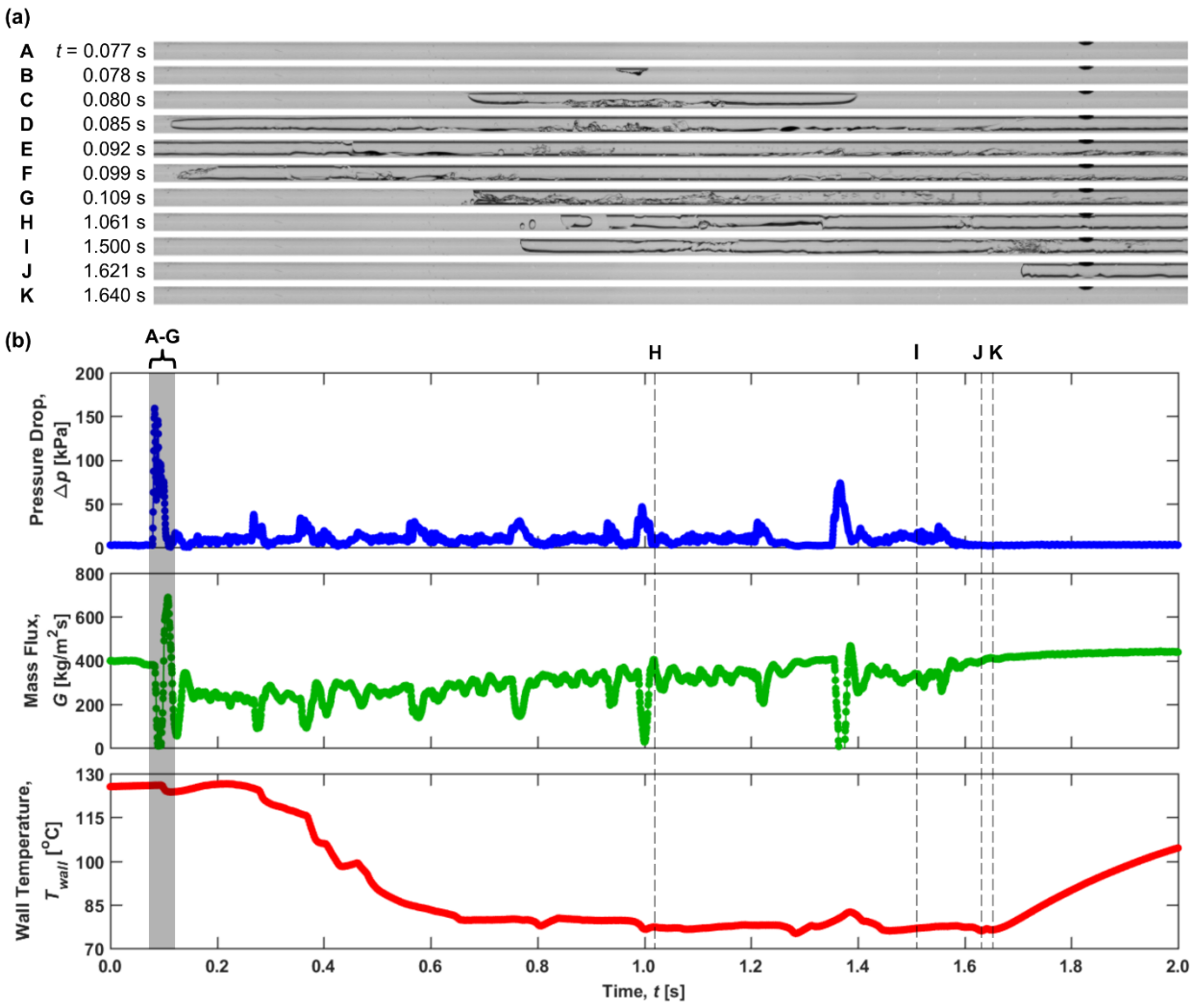

Figure 4. (a) Selected images of the two-phase morphology during the rapid-bubble-growth instability at the onset of boiling for $G_{1\phi}$ = 400 kg/m^{2}s and ΔT_{sub} = 15 °C, and (b) synchronized measurements of pressure drop, mass flux, and wall temperature. Images A-K in (a) correspond to the time instances indicated by the gray box (A-G) and dashed vertical lines (H-K) in (b). A corresponding video of the synchronized flow visualizations and thermal-fluidic signatures during the onset of boiling is available online in the Supplementary Materials (Video S4).

Similar to the prior case at the lower inlet liquid subcooling of ΔT_{sub} = 5 °C, vapor bubble nucleation from the channel surface (Figure 4; t = 0.078 s) is accompanied by explosive growth

both upstream and downstream causing the vapor bubble to occupy most of the channel (Figure 4; t = 0.092 s). A large pressure spike and a reduction in mass flux are observed (Figure 4b). A zero mass flux is detected by the flow meter at t = 0.089 s (Figure 4b), which lasts for 0.006 s, a reduction in time relative to the smaller inlet liquid subcooling of ΔT_{sub} = 5 °C (at which the zero mass flux reading lasted for 0.015 s). As a result, a minimal wall temperature increase of 0.5 °C is observed, from the single-phase wall temperature of 126.0 °C to a maximum temperature of 126.5 °C at t = 0.218 s. Incoming liquid then quickly replenishes the channel (Figure 4; t = 0.099 s) and cools (Figure 4b) the heated wall. The reduction in this duration of flow reversal likely results from the relatively cool incoming liquid minimizing the upstream propagation of the evaporating vapor-liquid interface.

After the onset of boiling, the mass flux slowly increases (~0.25 s < t < ~1.55 s) while the fluid is boiling (Figure 4; t = 1.061 s and t = 1.500 s). Eventually, the furthest upstream portion of the vapor-liquid interface is pushed downstream (Figure 4; t = 1.621 s) and the channel transitions to a single-phase flow regime (Figure 4; t = 1.640 s). A subsequent increase in the wall temperature is observed (Figure 4b). This cyclical process, namely, single-phase flow, boiling incipience, rapid-bubble-growth instability, and return to single-phase flow, marks the start of time-periodic flow boiling, which is discussed in Part 2 (Kingston *et al.*, 2017) of this two-part study.

When the inlet liquid subcooling is increased further to ΔT_{sub} = 35 °C, the high inlet subcooling minimizes the effect of the rapid-bubble-growth instability. While local flow reversal is still observed in the channel at the onset of boiling and results in a reduction in mass flux, the flow meter never detects a value of zero, indicating that the local flow reversal observed within the channel does not propagate upstream to the flow meter. A small increase in the wall

temperature is observed shortly after the onset of boiling, similar to the cases for ΔT_{sub} = 5 °C and 15 °C, before reducing to a much lower value during flow boiling conditions. A video showing the two-phase morphology synchronized to pressure drop, mass flux, and wall temperature measurements at the onset of boiling for a nominal single-phase mass flux of 400 kg/m^{2}s and inlet liquid subcooling of 35 °C is provided online in the Supplementary Materials (Video S5).

4 Conclusions

A constant pressure source was used to deliver fluid flow through a single microchannel subjected to a uniform heat flux while synchronized high-speed flow visualization and high-frequency pressure, mass flux, and temperature measurements were acquired. This deliberate design of the hydrodynamic boundary condition closely resembles that of an individual channel in a parallel-channel heat sink. The effects of nominal single-phase mass flux and inlet liquid subcooling on the rapid-bubble-growth instability is reported here in Part 1 of this study. The mechanisms underlying the rapid-bubble-growth instability, namely, large liquid superheat and a large pressure spike, were quantified and shown to result in flow reversal. Low flow inertia exacerbates the rapid-bubble-growth instability by starving the heated channel of liquid replenishment for longer durations and results in severe temperature increases. While flow reversal was also observed in the cases with high flow inertia, the wall temperature increase was minimal. The effect of the inlet liquid subcooling on the rapid-bubble-growth instability was small as indicated by the minimal increase in wall temperature. Flow reversal was observed for all three levels of subcooling, but higher subcoolings resulted in a shorter duration of flow reversal.

Acknowledgments

This research is sponsored by the Naval Engineering Education Consortium (NEEC), with support of Naval Surface Warfare Center (NSWC) Crane Division in Crane, Indiana. Special thanks to Dr. Brian D. Olson (NSWC Crane Division) for technical discussion of this work. Andrey E. Moskalenko assisted with constructing the test facility.

Supplementary Material

Supplementary material associated with this article can be found in the online version.

References

3M, 2002. 3M Novec Engineered Fluid HFE-7100 for Heat Transfer. 3M, St. Paul, MN, pp. 1-8.

Agostini, B., Fabbri, M., Park, J.E., Wojtan, L., Thome, J.R., Michel, B., 2007. State of the art of high heat flux cooling technologies. Heat Transfer Engineering, 28, 258-281.

Akagawa, K., Kono, M., Sakaguchi, T., Nishimura, M., 1971. Study on distribution of flow rates and flow stabilities in parallel long evaporators. Bulletin of Japan Society of Mechanical Engineers, 14, 837-848.

Bar-Cohen, A., Arik, M., Ohadi, M., 2006. Direct liquid cooling of high flux micro and nano electronic components. Proceedings of the Institute of Electrical and Electronics Engineers, 94, 1549-1570.

Barber, J., Brutin, D., Sefiane, K., Gardarein, J.L., Tadrist, L., 2011. Unsteady-state fluctuations analysis during bubble growth in a “rectangular” microchannel. International Journal of Heat and Mass Transfer, 54, 4784-4795.

Barber, J., Sefiane, K., Brutin, D., Tadrist, L., 2009. Hydrodynamics and heat transfer during flow boiling instabilities in a single microchannel. Applied Thermal Engineering, 29, 1299-1308.

Bergles, A.E., Kandlikar, S.G., 2005. On the nature of critical heat flux in microchannels. Journal of Heat Transfer, 127, 101-107.

Bigham, S., Moghaddam, S., 2015. Microscale study of mechanisms of heat transfer during flow boiling in a microchannel. International Journal of Heat and Mass Transfer, 88, 111-121.

Boure, J.A., Bergles, A.E., Tong, L.S., 1973. Review of two-phase flow instability. Nuclear Engineering and Design, 25, 165-192.

Garimella, S.V., Harirchian, T., 2013. Microchannel heat sinks for electronics cooling, in: Bar-Cohen, A. (Ed.), Encyclopedia of thermal packaging - thermal packaging techniques. World Scientific Publishing Company.

Huh, C., Kim, J., Kim, M.H., 2007. Flow pattern transition instability during flow boiling in a single microchannel. International Journal of Heat and Mass Transfer, 50, 1049-1060.

Kakac, S., Bon, B., 2008. A review of two-phase flow dynamic instabilities in tube boiling systems. International Journal of Heat and Mass Transfer, 51, 399-433.

Kandlikar, S.G., Colin, S., Peles, Y., Garimella, S., Pease, R.F., Brandner, J.J., Tuckerman, D.B., 2013. Heat transfer in microchannels - 2012 status and research needs. Journal of Heat Transfer, 135, 091001.

Kingston, T.A., Weibel, J.A., Garimella, S.V., 2017. High-frequency thermal-fluidic characterization of dynamic microchannel flow boiling instabilities: Part 2 - Impact of operating conditions on instability type and severity, International Journal of Multiphase Flow (in review).

Koşar, A., Kuo, C.J., Peles, Y., 2006. Suppression of boiling flow oscillations in parallel microchannels by inlet restrictors. Journal of Heat Transfer, 128, 251-260.

Kuang, Y.W., Wang, W., Miao, J.Y., Yu, X.G., Zhuan, R., 2017. Theoretical analysis and modeling of flow instability in a mini-channel evaporator. International Journal of Heat and Mass Transfer, 104, 149-162.

Kuo, C.J., Peles, Y., 2008. Flow boiling instabilities in microchannels and means for mitigation by reentrant cavities. Journal of Heat Transfer, 130, 072402.

Prajapati, Y.K., Bhandari, P., 2017. Flow boiling instabilities in microchannels and their promising solutions - A review. Experimental Thermal and Fluid Science, 88, 576-593.

Rao, S.R., Houshmand, F., Peles, Y., 2014. Transient flow boiling heat-transfer measurements in microdomains. International Journal of Heat and Mass Transfer, 76, 317-329.

Ruspini, L.C., Dorao, C.A., Fernandino, M., 2010. Dynamic simulation of Ledinegg instability. Journal of Natural Gas Science and Engineering, 2, 211-216.

Ruspini, L.C., Marcel, C.P., Clausse, A., 2014. Two-phase flow instabilities: A review. International Journal of Heat and Mass Transfer, 71, 521-548.

Tuckerman, D.B., Pease, R.F.W., 1981. High-performance heat sinking for VLSI. Electron Device Letters, 2, 126-129.

Van Oevelen, T., Weibel, J.A., Garimella, S.V., 2017. Predicting two-phase flow distribution and stability in systems with many parallel heated channels. International Journal of Heat and Mass Transfer, 107, 557-571.

Wang, G., Cheng, P., 2008. An experimental study of flow boiling instability in a single microchannel. International Communications in Heat and Mass Transfer, 35, 1229-1234.

Zhang, T., Tong, T., Chang, J.-Y., Peles, Y., Prasher, R., Jensen, M.K., Wen, J.T., Phelan, P., 2009. Ledinegg instability in microchannels. International Journal of Heat and Mass Transfer, 52, 5661-5674.